Microscopy and Microanalysis (2022), **28**, 1321–1334
doi:10.1017/S1431927621000337

Microscopy AND Microanalysis

Original Article

The Nanostructure of the Oxide Formed on Fe–10Cr–4Al Exposed in Liquid Pb

Kristina Lindgren[1]*, Peter Dömstedt[2], Peter Szakalos[2] and Mattias Thuvander[1]

[1]Department of Physics, Chalmers University of Technology, Göteborg SE-412 96, Sweden and [2]Department of Chemistry, Royal Institute of Technology (KTH), Stockholm SE-100 44, Sweden

Abstract

An Fe–10Cr–4Al alloy containing reactive elements developed for application in high-temperature liquid lead environments was analyzed after exposure in 600 and 750°C lead with dissolved oxygen for 1,000–2,000 h. Atom probe tomography, transmission electron microscopy, and X-ray scattering were all used to study the protective oxide formed on the surface. Exposure at 750°C resulted in a 2-μm thick oxide, whereas the 600°C exposure resulted in a 100-nm thick oxide. Both oxides were layered, with an Fe–Al spinel on top, and an alumina layer toward the metal. In the 600°C exposed material, there was a Cr-rich oxide layer between the spinel and the alumina. Metallic lead particles were found in the inner and middle parts of the oxide, related to pores. The combination of the experimental techniques, focusing on atom probe tomography, and the interpretations that can be done, are discussed in detail.

Key words: atom probe tomography, FeCrAl, liquid lead, oxide, reactive elements

(Received 15 December 2020; revised 15 February 2021; accepted 7 April 2021)

Introduction

Over the last decades, an increasing number of new clean energy solutions have emerged to mitigate the greenhouse gas emissions. Such category of clean energy technologies includes concentrated solar power (CSP) and the next generation (Gen IV) of nuclear reactors. The CSP technology already exists on the grid and provides electricity on a commercial scale. Most commonly, current CSP designs use solar salts ($NaNO_3$–KNO_3) as heat transfer fluid (HTF). However, solar salts disintegrate at close to 600°C (Bradshaw et al., 2009), which limits the thermal conversion efficiency. By replacing the solar salts with a fluid that is stable at higher temperatures, for example, liquid lead, one could achieve higher operational temperatures and thus increase the efficiency.

Gen IV energy solutions provide multiple benefits to the current clean energy market such as stable energy production, increased safety features, and the ability to reuse nuclear waste through recycling (Wallenius & Bortot, 2018; Wallenius, 2019). Lead-cooled fast reactors (LFRs) use lead as HTF and are one type of Gen IV reactor that has established fundamental improvements in terms of safety and performance, when compared with commercial water reactors. Lead is a natural gamma radiation shield and has the capacity of retaining harmful fission products, which otherwise could have been released to the surroundings if the multiple safety barriers were to be breached. Also, due to the large density change of lead with temperature, natural circulation will occur and thus maintain cooling of the reactor core in case of station blackout (Wallenius et al., 2012). However, a major drawback of using liquid lead as HTF is the corrosive nature and it imposes on the structural components. Construction steels typically rely on the formation of a chromia (Cr_2O_3) layer to protect the material from any kind of corrosion attacks. In a lead-based reactor, where temperatures are high, the chromia scale will no longer be sufficient or stable enough to be a reliable corrosion barrier. This is especially true with lead temperatures going above 550°C as it may cause critical oxidation and metal dissolution of the steels (Müller et al., 2002; Lambrinou et al., 2014; Ejenstam & Szakalos, 2015).

Alumina-forming ferritic steels, primarily FeCrAl, have shown superior oxidation properties in many extreme and high-temperature environments (Asher et al., 1977; Müller et al., 2002; Heinzel et al., 2006; Hattendorf et al., 2008; Zhang, 2009; Lim et al., 2010, 2013; Weisenburger et al., 2011; Fetzer et al., 2012; Ejenstam et al., 2013, 2015, 2017; Pint et al., 2014; Weisenburger et al., 2014; Ejenstam, 2015; Ejenstam & Szakalos, 2015). Therefore, these types of alloys are often proposed as material solutions in many high-temperature applications. Commercial FeCrAl steels are typically alloyed with Cr at high concentrations (13–23 wt%), which renders them susceptible to phase separation issues, known as *475°C embrittlement*. To avoid this embrittlement, a lean alloyed FeCrAl steel was previously developed, containing 10 wt% Cr and 4 wt% Al, using Ti, Nb, and Zr as reactive elements (REs) to optimize the oxidation properties for high-temperature lead environments. The addition of RE is known to significantly improve the oxidation properties, mainly by

*Author for correspondence: Kristina Lindgren. E-mail: kristina.lindgren@chalmers.se
Cite this article: Lindgren K, Dömstedt P, Szakalos P, Thuvander M (2022) The Nanostructure of the Oxide Formed on Fe–10Cr–4Al Exposed in Liquid Pb. *Microsc Microanal* **28**, 1321–1334. doi:10.1017/S1431927621000337

balancing the outward Al diffusion and the inward O diffusion through the oxide (Hultquist et al., 2001), as well as gettering of impurities (Hou & Stringer, 1992; Smialek et al., 1994). This type of Fe–10Cr–4Al+RE (10-4) alloy has, in previous studies, shown promising oxidation properties and ductile behavior in liquid lead up to 800°C (Dömstedt et al., 2019, 2020).

In order to fully understand the oxidation properties, the formation, and thus the structure, of the oxide formed on the alloy needs to be characterized. Atom probe tomography (APT) is a high-resolution characterization technique that can be used to analyze both conductive materials such as metals and, due to the laser-pulsed analysis, semiconductors, and insulators such as oxides (Larson et al., 2008; Stiller et al., 2012; Chen et al., 2014; Miller & Forbes, 2014). APT analysis of oxides is, however, challenging. The brittle oxides can fracture easily, making data collection something of a challenge. The presence of molecular ions in the mass spectrum makes the evaluation hard, due to overlaps, and thus, careful deconvolution of peaks is needed. In addition, oxides containing more than one cation can make the overlap issue even more challenging. This paper is focused on characterization, and the details of the oxide formed on the 10-4 alloy when exposed to liquid lead at 600°C are analyzed using APT. The results are compared with data from transmission electron microscopy (TEM), and energy-dispersive X-ray spectroscopy (EDX) of the alloy aged at the same conditions. Furthermore, the same alloy exposed to 750°C liquid lead is analyzed using STEM/EDX, as a comparison to the lower temperature that is closer to the intended operating temperatures. It was also possible to analyze the thicker oxide formed at 750°C by X-ray diffraction (XRD), to identify the phases of the oxide. These complimentary techniques make it possible to study the oxide formed in detail.

Materials and Methods

Material

The alumina-forming ferritic material, 10-4, was produced in a vacuum induction furnace. The heat was hot rolled at 1,100°C, followed by homogenization at 1,050°C. Samples were cut into roughly $30 \times 12 \times 2$ mm^3 coupons and sanded with 500 grit (US #360) SiC grinding paper. The sanded samples were then cleaned with ethanol and deionized water. The nominal composition of the 10-4 steel can be seen in Table 1.

Liquid Lead Exposures

The liquid lead corrosion tests were carried out in a tube furnace. Samples were placed in alumina crucibles filled with lead and placed inside a sealed quartz glass tube located in the furnace. The system was flushed with an Ar–5%H_2 gas mixture at the inlet for roughly 24 h before initiating the experiment. To achieve the desired oxygen activity at the set temperature, water vapor was added to the gas mixture. The gas mixture yields an H_2/H_2O ratio that can be translated into the amount of dissolved oxygen in the liquid lead. The oxygen content in the gas was measured at the outlet of the furnace using a ZIROX SGM5 oxygen sensor. For more information about the experimental setup and how the dissolved oxygen content is estimated can be found elsewhere (Müller et al., 2000, 2003; Ejenstam, 2015). Two exposures were performed in liquid lead, at 600°C for 1,080 h and at 750°C for 1,960 h. The 10-4 sample from the 750°C exposure has previously been investigated (Dömstedt et al., 2019) but will be studied in more detail in this work. To remove residual lead, samples were immersed into a solution consisting of hydrogen peroxide (H_2O_2), acetic acid ($C_2H_4O_2$), and deionized water with the ratios of 1:1:7 for 1 h. The parameters used and the measured oxygen activities at the outlet for the two exposures can be seen in Table 2.

Table 1. Composition of the 10-4 Steel, Given Both in wt.% and at.%.

Composition	Fe	Cr	Al	Si	C	RE
wt.%	86	10.0	4.0	0.15	<0.02	Ti + Nb + Zr = 0.3
at.%	82	10.2	7.9	0.3	<0.09	Ti, Nb, Zr

Reactive elements in the material is denoted as RE.

Table 2. Parameters Used, Estimated and Measured, for the Two Liquid Lead Exposures.

Exposure temperature (°C)	H_2/H_2O ratio	Dissolved O in Pb (wt%)	Measured pO_2 at outlet (bar)	Exposure time (h)
600	0.3	10^{-6}	1×10^{-23}	1,080
750	0.9	10^{-6}	3×10^{-20}	1,960

Characterization Techniques

The specimen preparation for APT and TEM was done using standard lift-out methods in an FEI Versa 3D focused ion beam/scanning electron microscope (FIB/SEM) (Larson et al., 1999; Langford & Petford-Long, 2001; Thompson et al., 2007). Prior to the lift-out, the oxide was coated with a few nanometre of Pd in order to avoid charging. In some cases, an additional layer of ~70 nm Au was deposited on top of the Pd, to be used as a marker during final thinning to obtain the top part of the oxide in the APT specimen.

Scanning TEM (STEM) was performed in an FEI Titan 80-300 operated at 300 kV, using both high-angle annular dark-field (HAADF) and bright-field (BF) detectors. The instrument is equipped with an Oxford X-sight EDX detector, and the TIA software was used for EDX evaluation.

For diffraction, a Bruker D8 Advance and a Mat:Nordic small-angle X-ray scattering/wide-angle X-ray scattering/gracing incidence small-angle scattering (SAXS/WAXS/GISAXS) system (SAXSLAB) were used, both with Cu-radiation sources.

APT was performed in a LEAP 3000X HR (Imago Scientific Instruments) with a green laser (532 nm wavelength). The pulse frequency was 100–200 kHz, and the laser energy was 0.3–0.7 nJ. The temperature was set between 30 and 70 K. For the oxides, the higher laser energies (0.5–0.7 nJ) and temperatures (60–70 K) were used for most of the analyses, as the lower ones resulted in premature fracture and thus short runs. This affects the mass spectra, giving more complex ions and wider thermal tails, and higher background (Kirchhofer et al., 2014), but makes it possible to get datasets large enough to contain multiple types of oxides and features.

The APT data were reconstructed using the commercial software IVAS 3.6.14 (Cameca). Parameters for the reconstruction of the APT data were varied dependent on the location of the analysis. In the metal, the evaporation field during analysis was estimated to 23 V/nm and a field factor (k) of 4.5 was used. For the oxides, the field was set to 27 V/nm, and k was set to a value so that the reconstructed thickness of the oxide layers was

https://doi.org/10.1017/S1431927621000337 Published online by Cambridge University Press

not too large, as the total thickness of the oxide was known from TEM. For the reconstruction of all analyses, the image compression factor used was 1.65.

Results

The exposure at 600°C resulted in the formation of a thin oxide of high quality, which was analyzed by APT and STEM/EDX. The oxide formed during exposure at 750°C was thicker and contained some larger pores, making it less suitable for APT. The higher thickness, on the other hand, made XRD and electron diffraction feasible, which were performed in addition to STEM/EDX. In this section, the results are presented in the order of technique used, starting with X-ray diffraction, followed by STEM/EDX and APT.

X-Ray Diffraction

The material exposed to lead at 750°C was analyzed using XRD and grazing incidence X-ray scattering. The oxide of the material exposed in 600°C was too thin to give any significant contribution to the scattering. In the θ–2θ setup (Fig. 1a), the substrate gave a few reflections due to the small size of the specimen. However, the ferritic metal and the Al_2FeO_4 spinel could both be confirmed in the diffractogram (see Fig. 1b for a smaller part of the diffractogram). When performing grazing incidence (GI) diffraction at 1° and 5° incidence angles, the same two phases were found (Fig. 1c). The shape of the peaks is somewhat widened due to the geometry of the specimen; the small size and the low angle made it hard to hit only the top surface of the specimen. The spinel peak at roughly 45° can be distinguished from the ferrite peak in the XRD diffractogram, but not in the GI diffractogram due to broadening of the peaks. In addition to the ferrite and spinel, small peaks corresponding to γ-Al_2O_3 were found in this more surface-sensitive setup.

Transmission Electron Microscopy

A STEM micrograph of the steel exposed at 750°C for 1,970 h can be seen in Figure 2a. The oxide scale thickness is ranging from 1.8 to 2.1 μm. There is a top layer rich in Al and Fe, with visible columnar grains, marked i) in the figure, with a grain width around 0.5 µm. This layer does not contain any Pb. Electron diffraction confirms that this is a spinel (Figs. 2b, 2c), presumably Al_2FeO_4 when considering the Fe/Al ratio measured by EDX (Table 3).

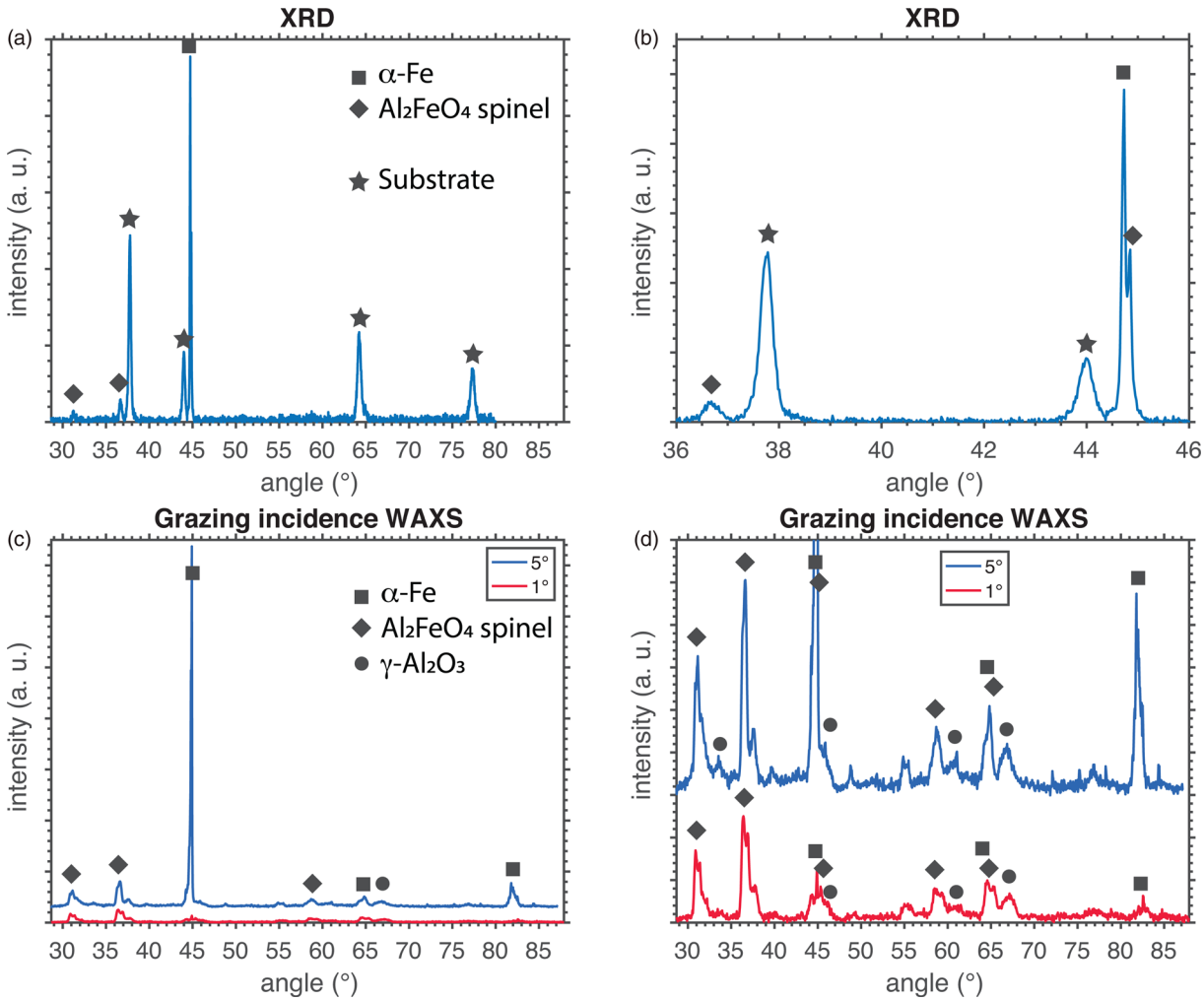

Fig. 1. X-ray diffraction of the material exposed in 750°C Pb. (**a**) A θ–2θ geometry was used for measurement. (**b**) A shorter part of the same diffractogram is shown. (**c**) Grazing incidence of 1° and 5° was used. (**d**) The same data as (**c**), but with a smaller range on the *y*-axis. and ((**c** and **d**) The 5° spectrum is shifted upwards in order to facilitate comparison.

https://doi.org/10.1017/S1431927621000337 Published online by Cambridge University Press

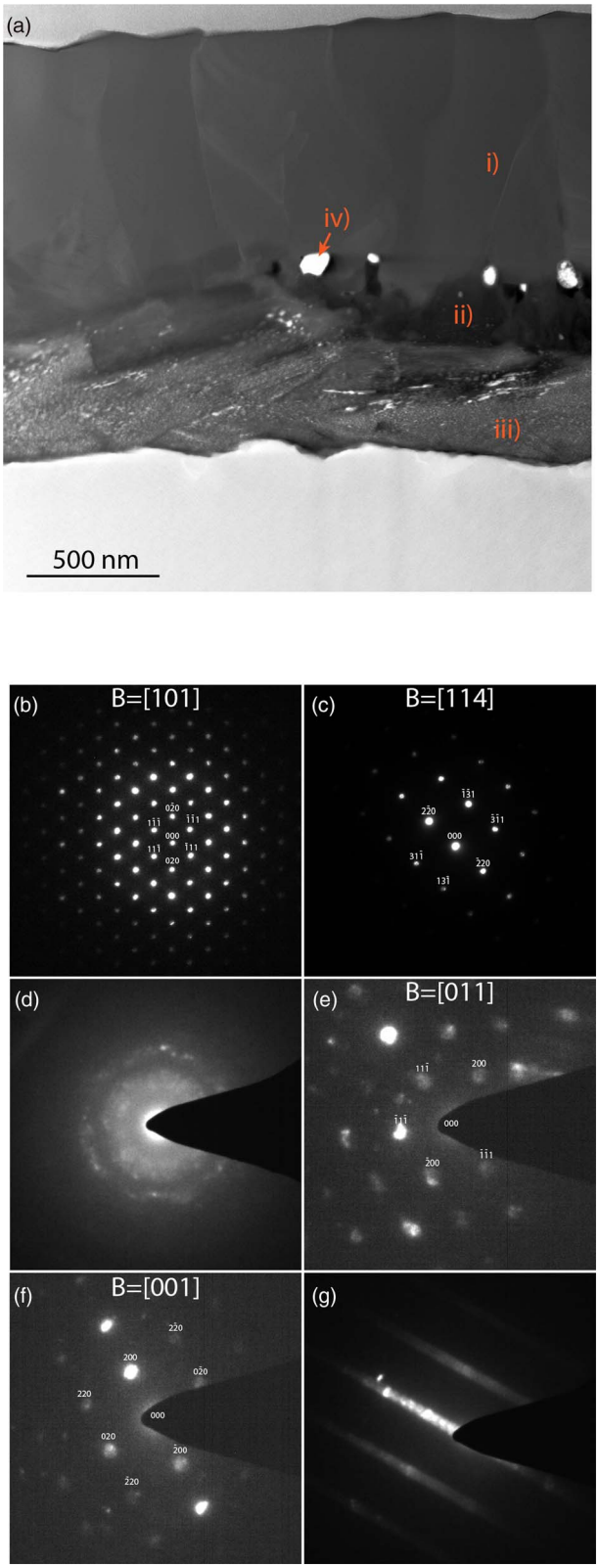

Fig. 2. (**a**) STEM-HAADF of the 750°C exposed material with marked locations for EDX analysis. (**b** and **c**) Indexed diffraction patterns of the top spinel layer, marked i) in (**a**). (**d**) The Al-rich oxide close to the metal, also containing Pb-rich nanocrystals, and (**e–g**) also from this layer (marked iii) in (**a**), but slightly further away from the metal.

Table 3. Metallic Compositions (Given in Normalized %) From EDX in Points Marked in Figure 2.

	Fe	Cr	Al	Pb	Ti
i)	34.8	0.2	65.0		
ii)	1.9	0.2	97.9		0.2
iii)	4.4	0.8	82.8	11.2	0.8

Larger amounts of oxygen were present in the EDX spectra but are removed in the normalization. Point iv) is not included in the table but was confirmed to be a Pb particle by EDX.

In the middle of the oxide, there is a dark contrast layer, that is, Al-rich (position ii) in Figure 2. The crystal structure of this layer is unknown. In this layer, there are Pb particles, marked iv) in the figure. These particles are in most cases in contact with dark contrast elongated features, that are interpreted as pores in the oxide. During the FIB lift-out sample preparation, there were pores visible in this middle layer, supporting this interpretation.

The inner oxide layer, closest to the metal substrate, is also Al-rich but contains a considerable amount of Pb. This layer is marked iii) in Figure 2a. The brighter contrast in this layer comes from small Pb particles. The size of these particles varies between 5 and 50 nm, and some of them are elongated. EDX analysis gives a small amount of Ti in the inner layer (0.8 at.% of the cations). The oxide close to the metal does appear amorphous in some regions where the oxide penetrates the metal slightly when studied by electron diffraction (Fig. 2d). The exact location of this specific diffraction pattern is outside the representative area shown in Figure 2a. In this pattern, there are rings that belong to the nanocrystalline Pb particles, in a diffuse background, that suggest an amorphous Al-rich oxide. However, electron diffraction shown in Figures 2e and 2f of the Al-rich oxide confirmed a crystalline γ-Al_2O_3 structure in some parts of the Al-rich inner layer, typically in regions like the one marked iii) in Figure 2a. For some tilt-angles, the diffraction patterns for this oxide contain streaks rather than points, as shown in Figure 2g, suggesting a faulted structure, with double diffraction in certain directions. The Pb particles were present in the γ-Al_2O_3 grains giving the diffraction patterns shown in Figures 2e–2g, but the diffraction is too weak in comparison to the reflections from the γ-Al_2O_3 to show in the patterns.

The steel exposed at 600°C was also analyzed using TEM. The STEM-HAADF and STEM-BF images in Figures 3 and 4 reveal a 100-nm thick oxide, containing three different layers. The top layer is rich in Al and contains some Fe, as seen in the EDX profile i) and the EDX map ii) in Figure 5, all excluding O from the quantification. The top surface appears to be facetted, which was confirmed by SEM of the surface (Supplementary Fig. S1). Beneath this layer, a thin Cr-enriched layer is present. The Cr in the EDX map does not appear to be evenly distributed within the layer, possibly due to overlaps of different oxide layers within the thickness of the TEM lamella, or due to variations in the composition of this part of the oxide. In connection with this layer, there are larger Pb particles (bright contrast in the HAADF image in Fig. 3 and seen in the EDX profile i) in Fig. 5). It is interesting to note that the volume around the Pb particle in the EDX map appears to be enriched in Cr and depleted in Al. Surrounding some of these particles is also a thin layer of dark

https://doi.org/10.1017/S1431927621000337 Published online by Cambridge University Press

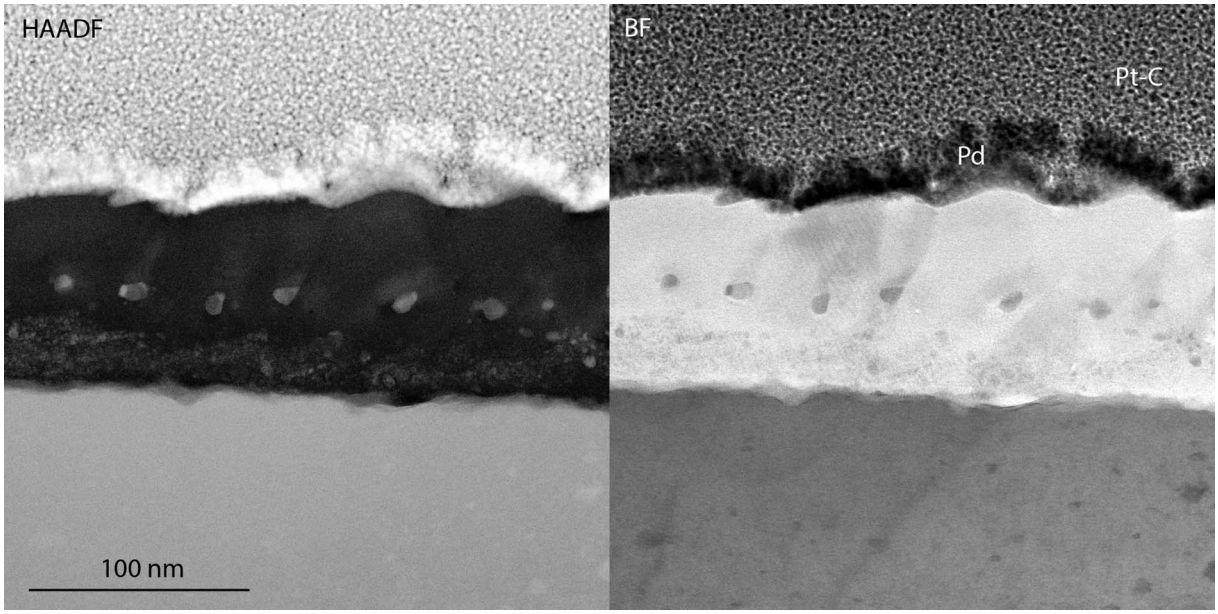

Fig. 3. 10-4 exposed in Pb at 600°C, STEM-HAADF and BF of the oxide.

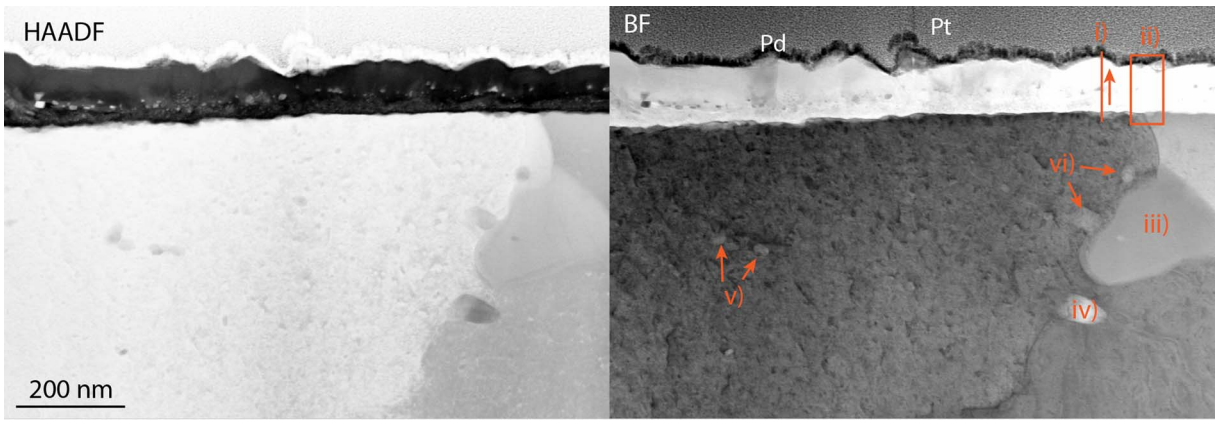

Fig. 4. HAADF and BF STEM of the 600°C exposed material, including references to the position and direction of the EDX line profile i), the position of map ii) (both in Fig. 5), and EDX spot analysis positions. iii) An intermetallic particle and iv)–vi) carbides.

contrast in the HAADF image, and bright contrast in the BF image (Fig. 3). At least some of these particles appear to be located in connection to grain boundaries of the top oxide layer. Under the Cr-rich layer, the oxide contains more Al, and only small amounts of Fe and Cr. This inner Al-rich oxide contains Pb particles that are smaller and more distributed than in the Cr-rich layer. These particles can be seen in the HAADF micrographs as bright spots and in the EDX map. In the metal–oxide interface, small amounts of RE (Nb, Ti, and Zr) were identified in the EDX map and profiles, as well as a few pores.

In Figure 4, a number of small carbides are seen in the metal, marked iv), v), and vi). According to EDX, they are rich in Nb and Ti, with the atomic Nb/Ti ratios of between 0.6 and 1.1. Two of them also gave a small Zr EDX-signal. Area iii) in Figure 4 contains 62.7% Fe, 20.0% Nb, 11.7% Ti, 5.0% Cr, 0.6% Al, and 0.1% Zr (at.%) and is presumably Laves phase, located in a grain boundary.

Atom Probe Tomography

The different types of oxide observed by TEM was also analyzed by APT for the thin oxide in the 600°C exposed material, giving three-dimensional information. A cross section of the top oxide is shown in Figure 6. The Al- and Fe-rich oxide does not contain any Pb particles. The figure also shows a thin layer containing Cr, in the bottom left of the analysis. This could possibly be a grain boundary, showing the complexity of the oxide in 3D. There is also a volume that contains slightly more Al and less Fe seen in the bottom right of the volume.

In Figure 7, a cut through an APT analysis heatmap of the Cr-rich layer and the Al-rich inner oxide is shown. In these layers, Pb particles are present. No other elements were found to segregate with the Pb, and therefore, the Pb particles are assumed to be purely metallic. Figure 7 shows that the interface between the two inner oxides also has a complex structure, with Cr extending into

https://doi.org/10.1017/S1431927621000337 Published online by Cambridge University Press

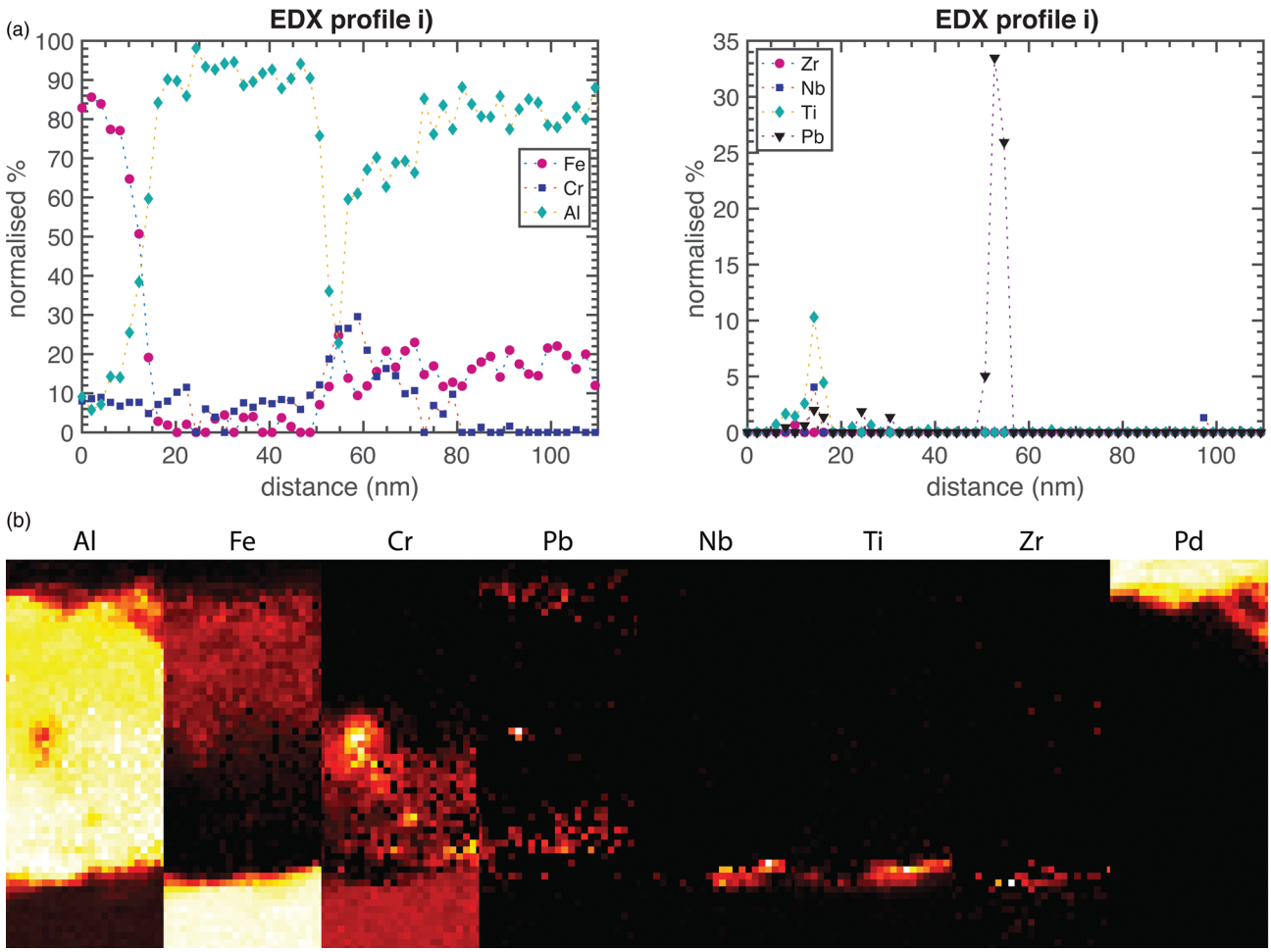

Fig. 5. EDX profiles and maps of the oxide formed at 600°C. The location of the maps is marked in Figure 4. The width of the EDX map is 50 nm. (**a**) An EDX line profile, normalized to exclude O, through the oxide thickness is shown. The oxide starts at 15 nm on the *x*-scale and is marked i) in Figure 4. (**b**) A map, marked ii) in Figure 4. The elements except O are shown individually.

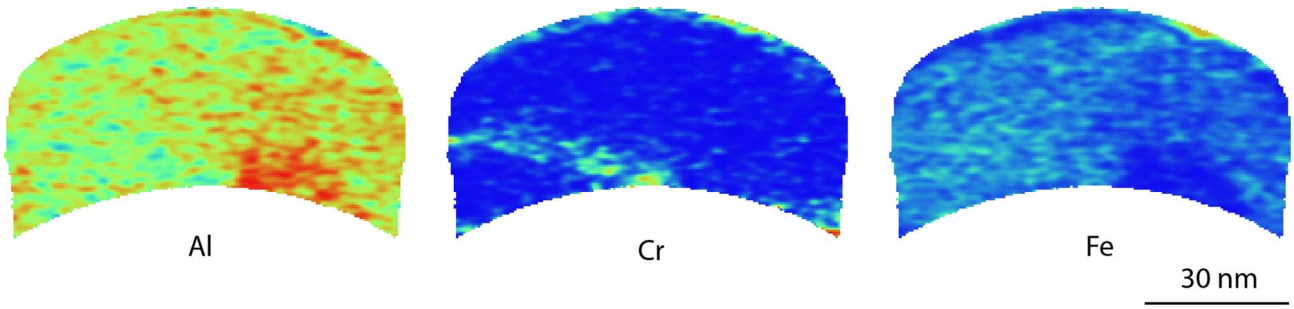

Fig. 6. Cross-section APT heatmap of Al, Cr, and Fe in the Al- and Fe-rich top oxide in material exposed at 600°C, showing concentration variations qualitatively. Red indicates high concentration and blue indicates low concentration. The peak at 27 Da was not used for these maps as there is an overlap between Al, Cr, and Fe.

the bottom oxide. The full shape of the reconstruction is based on the voltage curve, assuming the same evaporation field throughout the analysis. The change of composition is correlated with an increase in the diameter of the reconstruction. This increased diameter is mostly artificial, implying that the Al-rich oxide has a higher evaporation field than the Cr-rich oxide, thus needing a higher voltage to evaporate. The APT datasets shown do not contain any oxide/metal interfaces, due to the increased risk of specimen fracture during APT analysis in this region.

The mass spectra corresponding to the different parts of the oxides are shown in Figure 8. All three parts of the oxide contain Fe, Cr, and Al, contributing to the complex mass spectra, leading to several overlaps of molecular ions. The mass spectrum of the top Al–Fe-rich oxide contains wide peaks, due to the poor thermal conductivity and high laser pulse energy and temperature used. This spectrum is taken from a volume excluding the Cr-enriched boundary seen in Figure 6. The mass spectra of the Cr-rich volume (defined as the volume where the Cr

https://doi.org/10.1017/S1431927621000337 Published online by Cambridge University Press

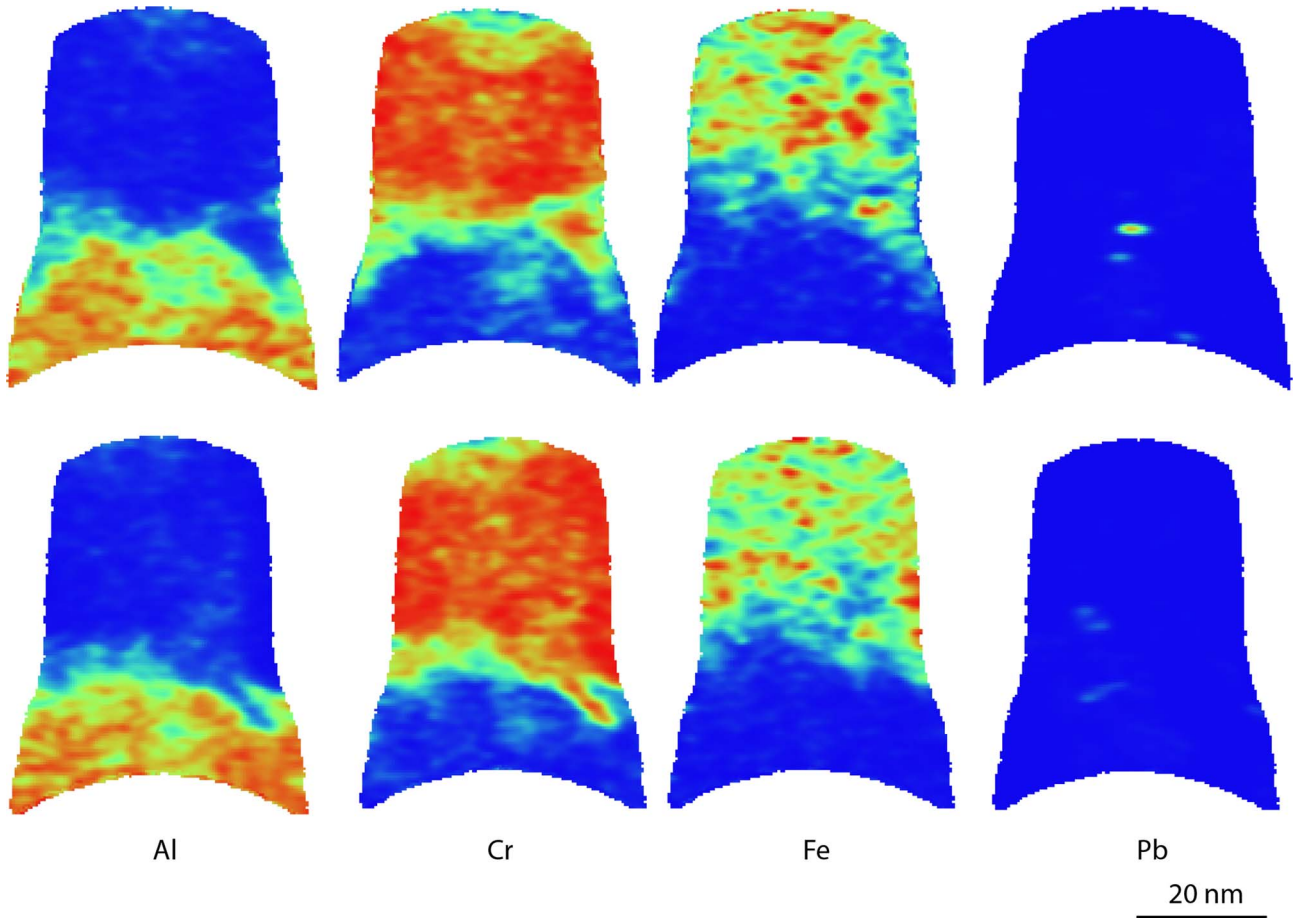

Fig. 7. APT cross-section heatmaps showing the qualitative distribution of Al, Cr, Fe, and Pb in the bottom two layers of the oxide from the material exposed at 600° C. Red indicates high concentration and blue indicates low concentration. The reconstruction was rotated by 90° between upper and lower rows of cross sections. The peak at 27 Da was not used for these maps as there is an overlap between Al, Cr, and Fe.

concentration is higher than 20 at.% in the analysis shown in Fig. 7) and the Al-rich volume (Al more than 20% in the same analysis) show more well-defined peaks, probably due to better heat transfer away from the tip apex during APT analysis. The heat transfer could also be improved by the short distance to the metal. The spectra contain many complex molecular ions and thus also overlaps. Some peaks correspond to different ions in different volumes, such as the 27 Da peak that was found to be 99.5% Al^{+} and 0.5% Fe^{2+} in the Al-rich oxide, but 54% Fe^{2+}, 45% Al^{+}, and 1% Cr^{2+} in the Cr-rich oxide, using deconvolution based on the natural abundance of isotopes. This shows the importance of a careful evaluation of each type of oxide separately.

From these mass spectra, the compositions were determined, as seen in Table 4. The largest possible error is misidentification of ions, particularly in the Al–Fe-rich oxide, where the peaks are wide and might obscure smaller contributions. Extra care was taken to find REs in the oxides. The only RE found was Ti (as TiO^{2+} at 31–33 Da) in the Al-rich and the Cr-rich oxide, see Figure 9. The mass spectrum of the Al–Fe-rich oxide contained too much background and too wide peaks to see any traces of TiO^{2+}, so the possible presence of small amounts of Ti can neither be confirmed nor refuted. The main naturally occurring TiO^{2+} isotope overlaps with O_2^{+} at 32 Da, but the peaks at 31, 31.5, and 32.5 Da match the intensities well of TiO^{2+}, and the peak at 33 Da is slightly higher, indicating an overlap with CrO^{2+}, see Figure 9. About 35 and 4% of the ions in the 32 Da peak correspond to TiO^{2+} in the Cr-rich and Al-rich oxides, respectively. The location of Ti in the oxide is not random, but not directly related to any obvious grain boundaries. The Ti in the Cr-rich oxide is mainly located close to the boundary to the inner Al-rich oxide. It is possible that a small part of the 32 Da peak also comes from S^{+} ions, possibly originating from the lead. However, this is assumed to be a small contribution, which can hardly be confirmed by APT, and is not included in the analysis.

The compositions in Table 4 should be interpreted as tentative values but show a composition corresponding well to the ones obtained by EDX (profile i) in Figure 5, considering the Al–Fe-rich and Al-rich oxides. The middle Cr-rich oxide contains more Cr in the APT data, but this might be due to varying composition or overlaps in the TEM lamella, as the EDX map (Fig. 5b) shows a varying Cr content in this layer. There are a few unidentified peaks, corresponding to 0.3–1.7% of the total number of ions. The Al-rich oxide contains only 0.3% ions in unidentified peaks. The Cr-rich oxide contains 1.7% unidentified ions, if the 27.5 Da peak is assumed to be Mn^{2+} (resulting in a total of around 0.4 at.% Mn in this part of the oxide). This is not included in the table as Mn only has one naturally occurring isotope, making the identification somewhat uncertain. This would also mean that the Mn is enriched in the oxide, when comparing with the average of 0.08 ± 0.02 at.% Mn in the bulk according to APT analysis of the metal (see below).

https://doi.org/10.1017/S1431927621000337 Published online by Cambridge University Press

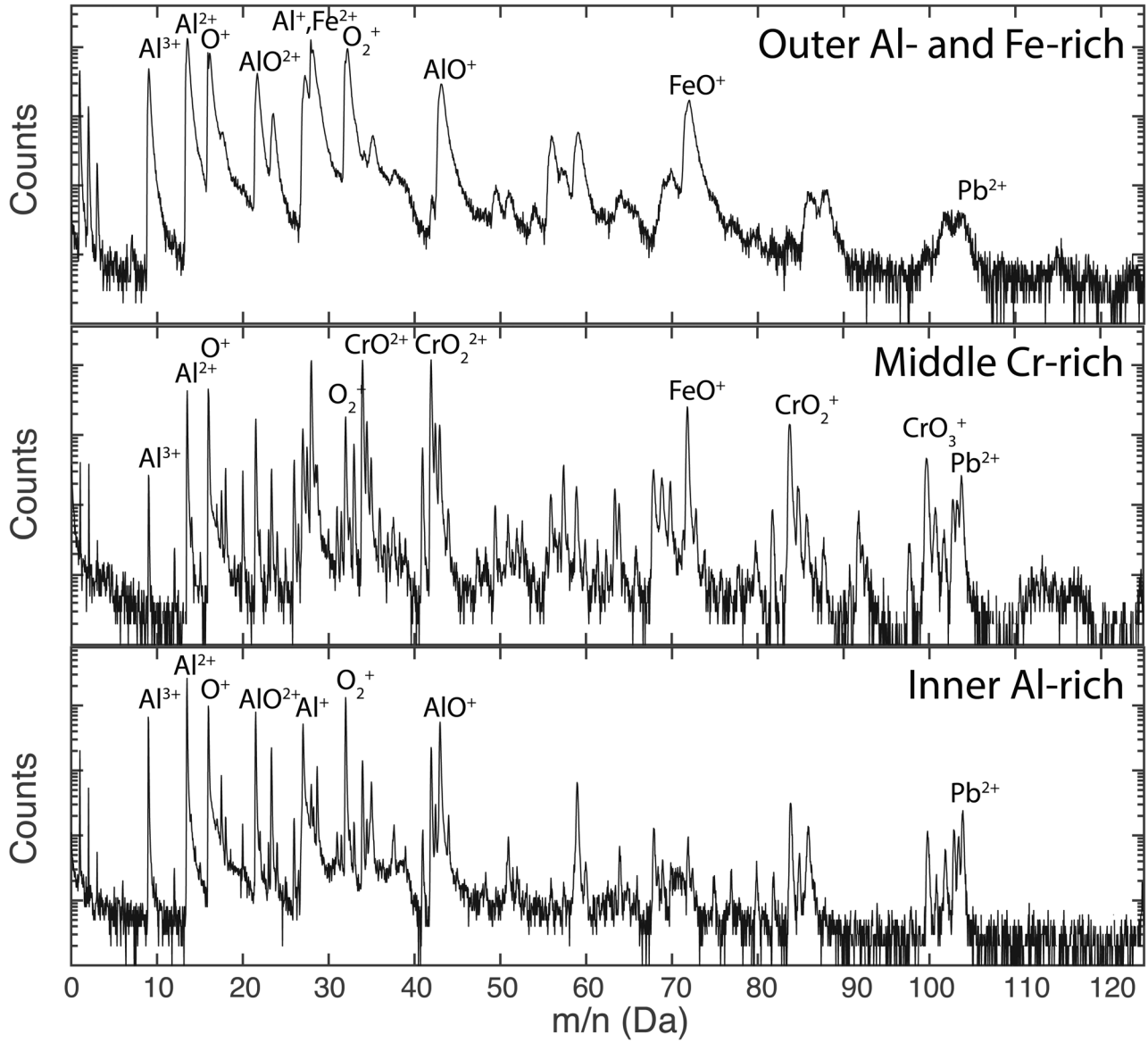

Fig. 8. Mass spectra from the different parts of the oxides of the 600°C exposed 10-4, as shown in Figures 6 and 7. The identity of some of the major peaks is marked. The scale on the *y*-axis is logarithmic.

The analysis shown in Figure 7 is also shown in Figure 10, where the entire volume is shown, and the Pb particles are outlined using iso-concentration surfaces chosen as Pb 7.9 at.%. Some of the Pb particles have volumes of high density in connection with them, sometimes connecting two particles. These high-density volumes are interpreted as pores. When a pore appears in an APT analysis, the edges of the pore will affect the direction of field evaporation, focusing or spreading the ions of the surrounding material into the volume corresponding to the pore, depending on the local evaporation field close to the pore (Krämer et al., 2017; Lloyd et al., 2019; Wang et al., 2020). This effect often results in an artificially high ionic density in the reconstructed volume.

Table 4. Measured Compositions of the Oxides in the 600°C Exposed Material, From APT (at.%).

	O	Al	Cr	Fe	Pb	Ti
Al–Fe-rich	51	34	0.2	15	0.03	–
Cr-rich	54	5	27	14	0.6	0.6
Al-rich	52	41	5	1	0.7	0.6

Oxygen is most likely somewhat underestimated.

A slice of the same analysis, showing the Pb atoms and some of the oxide ions, is shown in Figure 11. Here, it is seen that the Pb atoms have evaporated into plates. The arrows in the figure are perpendicular to the curvature of the evaporating surface. An assumption is that this is an indication of the Pb particles having much lower evaporation field than the surrounding material. Thus, when the material above the particle is evaporated, most of the Pb will evaporate immediately, resulting in the disc-shaped particles in the reconstruction. This can be compared with similar effects from pores containing Xe observed by Estivill et al. (2016). In Figure 11, it can also be seen that there are some unevenly distributed Pb atoms in the oxide.

https://doi.org/10.1017/S1431927621000337 Published online by Cambridge University Press

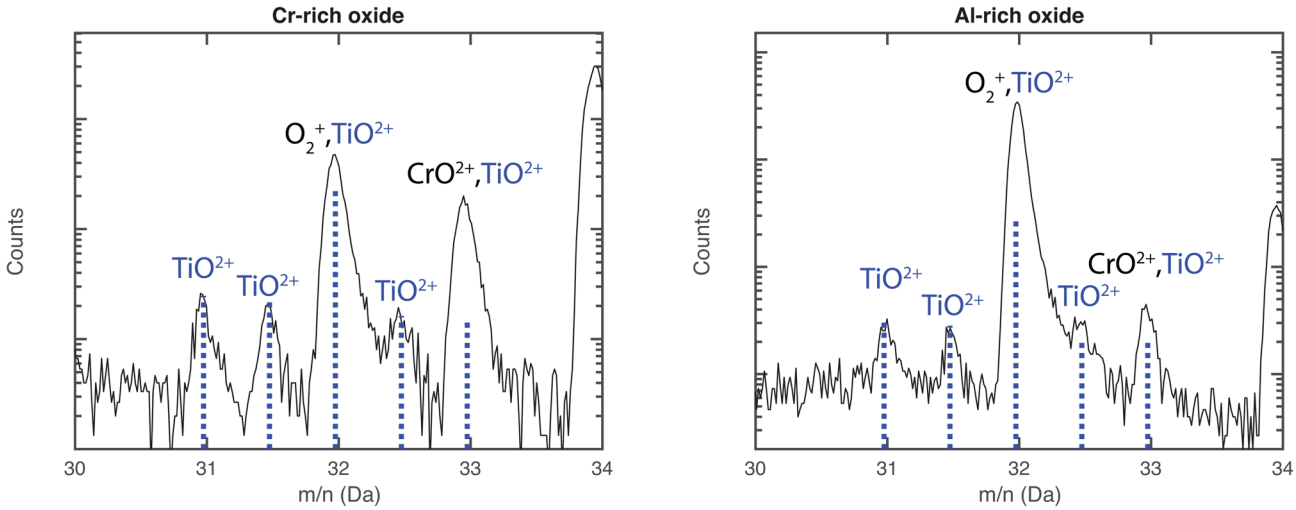

Fig. 9. Mass spectrum from 30 to 34 Da for the middle Cr-rich and bottom Al-rich oxide layers of the 600°C exposed material. The natural abundance of TiO^{2+} is marked in blue (fitted for 31 Da), overlapping with O_2^+ and CrO^{2+}. The peak at 34 Da is the main peak of CrO^{2+}.

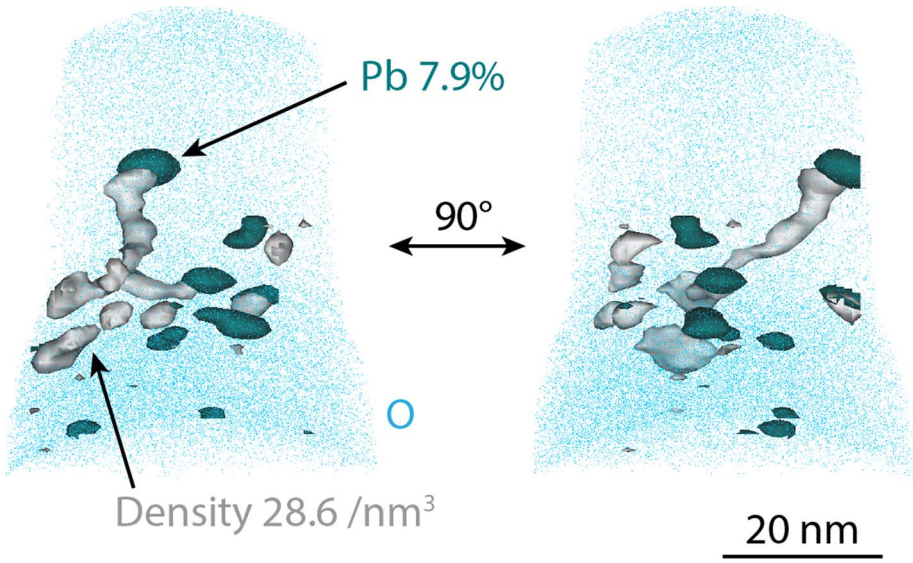

Fig. 10. Pb particles in the 600°C exposed material, visualized by 7.9 at.% Pb iso-concentration surfaces, and high-density volumes in connection with them, showed as 28.6 atoms/nm^3 iso-density surfaces (corresponding to 77.3 atoms/nm^3 when correcting for the detection efficiency of the LEAP). O atoms in blue show the extension of the analysis. The analysis is shown fin two different directions. This is the same analysis that is shown in Figure 7.

A few carbides in the metal were also analyzed by APT. One was found to sit on a grain boundary enriched in Nb, Zr, Ti, Si, and B, see Figure 12. Note that the APT analysis in question was run in laser pulsed mode, and thus, the Si distribution should be interpreted with some care, as Si moves on the surface when exposed to the laser beam (Gault et al., 2010; Hyde et al., 2011). In another APT reconstruction (not shown here), three carbides were present, within a distance of 50 nm from each other, and not apparently close to any enriched boundary. The APT of the carbides confirms the Ti- and Nb-rich composition given by STEM/EDX. In the carbides, the Nb/Ti ratios (in at.%) varied between 0.51 and 0.74 in the carbide in the figure and the three carbides in the other analysis. The carbides also include small amounts of Zr (0.4–2 at.%). The carbides are assumed to be of MC type, where typically the measured C content in APT (43 at.% when not corrected in the carbides here) is a bit lower than expected due to multiple events during field evaporation (Thuvander et al., 2011). It is also possible that the carbides are slightly sub-stoichiometric. The carbides analyzed show slightly different compositions in terms of Ti, Nb, and Zr content, which is to be expected due to local variations in the material.

The metal matrix composition, as measured by APT, was found to match the expected composition in terms of the Cr content, see Table 5. The Al content was somewhat lower than expected, possibly due to migration to the oxide (the bulk analysis was done within a micrometer of the oxide) or varying content within the material. Small amounts of Nb, Ti, and Zr were measured in the metal matrix (0.004 ± 0.003, 0.14 ± 0.04, and 0.008 ± 0.005 at,%, respectively, where the error is the standard deviation between the four APT measurements used for composition determination).

https://doi.org/10.1017/S1431927621000337 Published online by Cambridge University Press

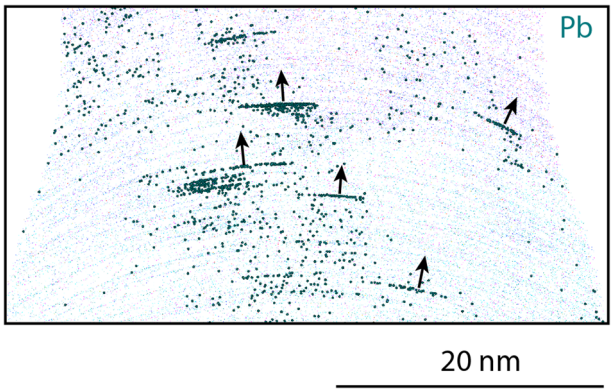

Fig. 11. A 5-nm thick slice of the APT reconstruction of the analysis in Figures 7 and 10 shows Pb atoms on layers in the 600°C exposed material. Ions belonging to the Al-rich oxide (blue) and Cr-rich oxide (pink) are also present to show the outline of the reconstruction. The arrows are perpendicular to the layers that follow the curvature of the needle during evaporation.

Discussion

In this paper, a detailed analysis of the oxides formed on a ferritic steel when exposed to lead at 600 and 750°C is presented. Here follows a discussion concerning the characterization of the oxide combining APT, TEM, and X-ray diffraction, as well as a few comments on the oxidation and corrosion properties of the material itself. The main focus of the discussion is the interpretation of the APT data, and the conclusions that can be made in combination with the other techniques.

APT Analysis of the Oxide Formed at 600°C

The oxide of a FeCrAl alloy exposed to lead at 600°C was successfully analyzed using APT. The cation composition corresponds well to the content as measured by STEM/EDX, except from the middle oxide layer that appears uneven in the EDX Cr-distribution, and thus possibly is overlapping with the inner and outer oxides in the TEM lamella, decreasing the Cr content in the EDX measurement. The correspondence between APT and EDX was generally good, despite the fact that green laser was used. It has been shown that a UV-laser gives a mass spectrum with lower background, fewer thermal tails and possibly fewer complex ions when analyzing oxides (Santhanagopalan et al., 2015; Boll et al., 2017). In the present study, this seems not to have had a significant influence on the measured compositions.

The outer oxides of both exposures are rich in Al and Fe and show a facetted surface (Supplementary Fig. S1). It was confirmed by diffraction that this oxide was Al_2FeO_4 spinel for the material exposed at 750°C, making it likely that the same oxide was formed also during exposure at 600°C. The phase constitution of the inner Al-rich oxide of the 600°C exposed alloy is unknown, but

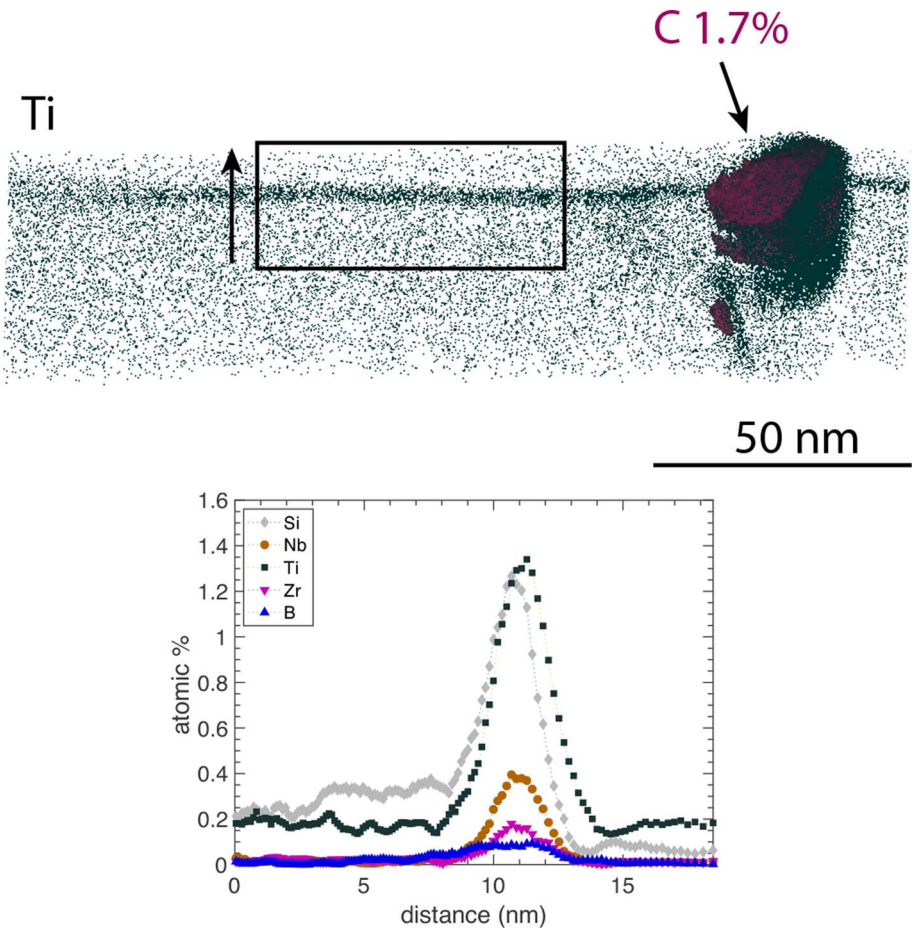

Fig. 12. A carbide in the 600°C exposed material, visualized by a C 1.7 at.% C iso-concentration surface, located at a grain boundary in the metal, aligned perpendicularly to the image plane. The full APT reconstruction is shown. The vertical arrow indicates the direction of the composition profile through the grain boundary.

https://doi.org/10.1017/S1431927621000337 Published online by Cambridge University Press

Table 5. Metal Composition, From APT Analysis of the Material Exposed in 600°C, Given in at.%.

Fe	Cr	Al	Mn	Si	C	V	B	Nb	Ti	Zr
Bal.	10.1 ± 0.1	6.6 ± 0.2	0.08 ± 0.02	0.24 ± 0.04	0.06 ± 0.04	0.002 ± 0.001	0.001 ± 0.001	0.004 ± 0.003	0.14 ± 0.04	0.008 ± 0.005

The error is the standard deviation between different analyses.

the 750°C material shows a combination of γ-Al_2O_3 and amorphous alumina.

The 51–54 at.% O in the oxides in the APT measurements (Table 4) can be compared with the possible phase Al_2O_3 containing 60 at.% O, and a spinel, M_3O_4, containing 57 at.% O. The O content of oxides is often observed to be too low when measured by APT (Maier et al., 2016). This might be due to a large fraction of multiple events (leading to detector pile-up), evaporation of O as neutrals, and dissociation of evaporated molecules that can make the O content deviate from the expected value (Karahka & Kreuzer, 2013; Liu & Stiller, 2013).

The possible presence of RE in the oxide is of interest. EDX could miss small quantities of RE as the number of counts in the spectra are limited due to the oxide being electron beam sensitive. APT can give compositions of trace elements with as low content as a few tens of ppm under favorable conditions. However, the peaks in the mass spectra of the 600°C formed oxide are wide, and there are some unidentified peaks, and with a number of possible molecular ions and overlaps, makes the mass spectrum evaluation complex, and thus, the detection limit is higher. Both Zr and Ti have a number of naturally occurring isotopes, giving them a distinct "fingerprint" in the spectra, which usually helps identification. Nb only has one naturally occurring isotope (^{93}Nb) and is thus harder to distinguish from other peaks in the mass spectra. By experience and observations from other materials, which ions are usually found in oxides containing Ti, Zr, or Nb, the following ions are typical examples of what was looked for in the mass spectra: Ti^+, Ti^{2+}, TiO^{2+}, TiO^+, $TiO_2{}^+$, Zr^{2+}, ZrO^{2+}, $ZrO_2{}^+$, Nb^+, Nb^{2+}, NbO^+, NbO^{2+}, and $NbO_2{}^+$. Out of these, TiO^{2+} was observed in the mass spectrum (Fig. 9). TiO^{2+} overlaps with Nb^{3+} at 31 Da, but this peak is probably mostly TiO^{2+} due to that the natural abundance was matching this peak well, see Figure 9. The Ti found using EDX in the Al-rich layer of the 750°C exposed sample supports the possibility of the inner oxide containing Ti. Nb and Zr were not observed in this EDX spectrum, nor in the APT data of the oxide of the alloy exposed at 600°C.

Dependent on the solubility of Ti in γ-Al_2O_3, and in amorphous alumina, different locations of Ti would be expected. In the case of RE in an oxide that does not dissolve any RE, like α-Al_2O_3, the RE are expected to be found in grain boundaries, as previously observed by APT (Chen et al., 2014; Boll et al., 2017; Unocic et al., 2018; Vayyala et al., 2020). In the oxide formed on FeCrAl studied in this paper, the Ti atoms appear not to be distributed randomly, but not in boundary layers or oxide particles either. In the oxide of the material exposed at 750°C, we know that the oxide is partly γ-Al_2O_3, and probably partly amorphous. For the 600°C case, the crystal structure of the Al-rich oxide is unknown, but possibly it is amorphous to a larger degree due to the lower exposure temperature. If the alumina does dissolve some Ti, the atoms can be evenly distributed in this oxide layer. Another possibility is that the oxide does not dissolve that much Ti, but is nanocrystalline, containing these RE in the grain boundaries, similar to what was observed in a FeCrAl alloy exposed to high temperature (900–1,000°C) O_2, H_2O, and/or N_2 (Mortazavi et al., 2018). However, the grains would have to be a few nanometers only for this to be a possibility, considering the observed Ti distribution.

APT Analysis of the Pb Particles

The Pb particles appear as ultra-thin discs parallel to the specimen surface in the APT reconstructions, but TEM supports that these actually are mostly spherical. The Pb particles are, thus, expected to have a much lower evaporation field than the oxide surrounding them. The Pb mostly evaporates as 2+ ions, although there are a few 1+ ions as well. No complex ions containing Pb were identified. Comparing the charge states with Kingham curves (Kingham, 1982), gives an indication that the field of the particles is close to the crossover of 1+ and 2+ ions, that is slightly higher than 20 V/nm. The field of the surrounding oxide is believed to be considerably higher than this, and 27 V/nm was used for the reconstruction. The applicability of the Kingham curves to laser-pulsed APT is, however, questionable. The fact that the Pb particles appear very flat indicates that all the Pb atoms from one particle were evaporated during a very short time span. Maybe the laser pulses even caused the small Pb particles to melt (the melting point of Pb is 600 K). It is not well known how nanometer-sized metallic particles in a nonconducting oxide are affected by the laser beam. In case the temperature increase of the Pb particles is high, the atoms are expected to evaporate easily, at a very low local field. The post-ionization, on the other hand, is mainly given by the field strength at a slightly larger scale, making it reasonable to obtain 2+ ions, even if the local field of the small particles might be lower than 20 V/nm.

Bursts of Pb and O in lead oxides ($Pb(Ti,Zr)O_3$) observed by Kirchhofer et al. (2014) indicate a low evaporation field also of lead oxide. In our case, O was not associated with the Pb particles. Furthermore, the Pb in the mass spectra of our materials did not evaporate as molecular ions including O (as was the case in the study by Kirchhofer et al.), supporting that the particles are metallic Pb rather than Pb oxide.

Pores

In the 750°C exposed material, the pores appearing in connection with the Pb particles are clearly visible in the TEM lamella, see Figure 2. In Figure 3, showing the 600°C material, there is some dark contrast around the largest Pb particles in the middle oxide layer in the HAADF image. The high-density volumes observed in the APT data are much smaller, and thus probably not possible to be observed in the TEM micrograph due to overlapping structures and a high density of small Pb particles in this part of the oxide. However, the occurrence of larger pores supports the interpretation of the high-density regions in the APT reconstructions as pores in the case of the smaller particles as well. The morphology seen in the STEM micrographs also

https://doi.org/10.1017/S1431927621000337 Published online by Cambridge University Press

supports the assumption that the Pb particles are solid, sitting inside the pore, rather than covering the inside of the pore as a shell or a hollow particle. Considering the size of the pores, Wang et al. (2020) observed that the size of the density variation volume within the APT reconstruction is similar to that of the pore in the oxide.

Open questions regarding the pores with Pb particles inside are their formation; when and why they are formed. Furthermore, it is possible that the pores impact the protectiveness and mechanical stability of the oxide. However, the effect is assumed to be small, as no spallation of the oxide was observed in the exposures.

Oxidation and Corrosion Properties

After exposure at 600°C for 1,008 h, the formed oxide is only around 100 nm thick with three identified layers. The outer facetted layer is rich in Al and Fe, which could be an Al_2FeO_4 spinel. The inner layer is an Al-rich oxide with small and distributed Pb particles and the middle layer is Cr-enriched with larger Pb particles. The Pb particles could have been encapsulated during the early stages of oxidation. The Cr-enriched oxide layer could represent the initial surface, assuming that the first oxide layer to be formed on the surface when the material is exposed is a mixture of Fe–Al–Cr oxides. The growth process would then be followed by an outwards growing spinel and an inwards growing Al-rich oxide. Similar observations were made by Ejenstam et al. (2013) on FeCrAl materials exposed to liquid lead at 550°C.

The REs in the 10-4 alloy were mainly identified in carbides in the metal, in metal grain boundaries, and at the oxide/metal interface. Smaller amounts of Ti were found in the inner Al-rich oxide layer for both exposure temperatures. Previous work by Ejenstam et al. (2017) showed that an excess amount of C in similar alloys as used in this study, promoted the formation of Cr-rich carbides at the surface, obstructing the formation of the Al-oxide. By balancing the RE addition with respect to the C content, the Cr-rich carbides could be suppressed and thus improving the oxidation properties. In this work, no Cr-rich carbides were identified but rather, small and distributed RE-carbides were observed. These RE-carbides are found throughout the metal substrate and are likely not disrupting the formation of the protective oxide. The different REs were identified at the metal–oxide interface, which could increase the adherence of the oxide by the so-called keying/pegging effect. While no clear evidence of any key-effect was noted in this work, the observation of such effect has previously been on the same type of 10-4 alloy (Dömstedt et al., 2020), as well as in other FeCrAl alloys with different RE additions (Golightly et al., 1976; Hindam & Whittle, 1982; Nowok, 1982). It is also possible that RE oxides are formed at the surface, which operate as nucleation sites for continued oxide growth (Josefsson et al., 2005), as well as limiting void formation beneath the oxide during growth (Pint, 1996).

When comparing the results from exposure of the same material at higher temperatures (800°C) in an earlier publication by Dömstedt et al. (2020), the oxide was slightly thicker (up to 5 μm) than the one formed at 750°C (2 μm) studied here, but qualitatively similar. Both exposures resulted in an Al–Fe-rich top layer and an Al-rich inner oxide. The outer Al_2FeO_4 spinel was of similar total thickness in the two exposures (around 1 μm). However, the inner Al-rich oxide was thicker in the 800°C exposed material, which indicates a more favorable formation of the alumina.

In conclusion, the different characterization techniques used in this study worked well to complement each other for the nanoscale characterization of an oxide formed during exposure to liquid Pb at high temperatures. STEM gave a good overview of the oxide in the case of the thick oxide formed at 750°C, and TEM diffraction made it possible to identify phases. The X-ray scattering helped identifying the phases of the thick oxide. However, more details of the complex small-scale structure of the 600°C exposure oxide could be revealed using APT. The complex structure of the small pores surrounding the Pb particles was clearer in the APT data, as well as the local compositions in the different parts of the oxide.

Conclusions

In this paper, the detailed microstructure of a Fe–10Cr–4Al–RE alloy exposed to liquid lead (with 10^{-6} wt% O dissolved) at 600 and 750°C has been explored by TEM, APT, and X-ray diffraction. It was found that:

- It is possible to analyze the oxide using APT, and get the compositions of different layers, in good agreement with TEM/EDX data, although there are many overlap issues in the APT spectra due to mixed oxides containing both Al, Fe, and Cr.
- The alloy performs well at 600°C—after 1,008 h a 100-nm oxide layer has formed that protects the surface.
- At 750°C, a thicker oxide (2 μm) was formed after 1,970 h.
- For both exposures, there was an Al-rich inner oxide and an outer Fe–Al spinel formed.
- At 600°C, a middle layer containing Cr in addition to Fe and Al was found. APT revealed that the most abundant cation in this oxide layer is Cr.
- Inside the middle and lower part of the oxide, there are metallic Pb particles, in many cases surrounded by pore structures. These were possible to analyze with APT in the case of 600°C, where the pores were small.

Supplementary material. To view supplementary material for this article, please visit https://doi.org/10.1017/S1431927621000337.

Acknowledgments

Kanthal, part of Sandvik Group, is acknowledged for the production of the material. Dr. Olof Bäcke and Dr. Mohammad Sattari at Chalmers are acknowledged for assistance with TEM. Prof. Krystyna Stiller and Mr. Pratik Lokhande at Chalmers are acknowledged for fruitful discussions, and Dr. Michal Strach for help with the diffraction measurements. The characterization was performed at Chalmers Materials Analysis Lab (CMAL).

Financial support. This work was funded by the Swedish Research Foundation (VR) within project 2017-06458.

References

Asher RC, Davies D & Beetham SA (1977). Some observations on the compatibility of structural materials with molten lead. *Corros Sci* **17**(7), 545–557.

Boll T, Unocic KA, Pint BA & Stiller K (2017). Interfaces in oxides formed on NiAlCr doped with Y, Hf, Ti, and B. *Microsc Microanal* **23**(2), 396–403.

Bradshaw RW, Cordaro JG & Siegel NP (2009). Molten nitrate salt development for thermal energy storage in parabolic trough solar power systems. *Energy Sustain* **48906**, 615–624.

Chen Y, Reed RC & Marquis EA (2014). Interfacial solute segregation in the thermally grown oxide of thermal barrier coating structures. *Oxid Met* **82** (5–6), 457–467.

Dömstedt P, Lundberg M & Szakalos P (2019). Corrosion studies of low-alloyed FeCrAl steels in liquid lead at 750 °C. *Oxid Met*. **91**, 511–524.

Dömstedt P, Lundberg M & Szakálos P (2020). Corrosion studies of a low alloyed Fe–10Cr–4Al steel exposed in liquid Pb at very high temperatures. *J Nucl Mater* **531,** 152022.

Ejenstam J (2015). *Corrosion Resistant Alumina-Forming Alloys for Lead-Cooled Reactors*. Stockholm: Kungliga Tekniska högskolan.

Ejenstam J, Halvarsson M, Weidow J, Jönsson B & Szakalos P (2013). Oxidation studies of Fe10CrAl–RE alloys exposed to Pb at 550°C for 10,000 h. *J Nucl Mater* **443**(1–3), 161–170.

Ejenstam J, Jönsson B & Szakalos P (2017). Optimizing the oxidation properties of FeCrAl alloys at low temperatures. *Oxid Met* **88**(3), 361–370.

Ejenstam J & Szakalos P (2015). Long term corrosion resistance of alumina forming austenitic stainless steels in liquid lead. *J Nucl Mater* **461**, 164.

Ejenstam J, Thuvander M, Olsson P, Rave F & Szakalos P (2015). Microstructural stability of Fe-Cr-Al alloys at 450-550 °C. *J Nucl Mater* **457**, 291.

Estivill R, Audoit G, Barnes JP, Grenier A & Blavette D (2016). Preparation and analysis of atom probe tips by xenon focused Ion beam milling. *Microsc Microanal* **22**(3), 576–582.

Fetzer R, Weisenburger A, Jianu A & Müller G (2012). Oxide scale formation of modified FeCrAl coatings exposed to liquid lead. *Corros Sci* **55**, 213–218.

Gault B, Müller M, La Fontaine A, Moody MP, Shariq A, Cerezo A, Ringer SP & Smith GDW (2010). Influence of surface migration on the spatial resolution of pulsed laser atom probe tomography. *J Appl Phys* **108**(4), 044904.

Golightly FA, Stott FH & Wood GC (1976). The influence of yttrium additions on the oxide-scale adhesion to an iron-chromium-aluminum alloy. *Oxid Met* **10**(3), 163–187.

Hattendorf H, Hojda R, Naumenko D & Kolb-Telieps A (2008). A new austenitic alumina forming alloy: An aluminium-coated FeNi32Cr20. *Mater Corros* **59**(6), 449–454.

Heinzel A, Kondo M & Takahashi M (2006). Corrosion of steels with surface treatment and Al-alloying by GESA exposed in lead–bismuth. *J Nucl Mater* **350**(3), 264–270.

Hindam H & Whittle DP (1982). Peg formation by short-circuit diffusion in Al_2O_3 scales containing oxide dispersions. *Electrochem Soc* **129**, 1147–1149.

Hou P & Stringer J (1992). Oxide scale adhesion and impurity segregation at the scale/metal interface. *Oxid Met* **38**, 323–345.

Hultquist G, Tveten B, Hörnlund E, Limbäck M & Haugsrud R (2001). Self-repairing metal oxides. *Oxid Met* **56**, 313–346.

Hyde JM, Burke MG, Gault B, Saxey DW, Styman P, Wilford KB & Williams TJ (2011). Atom probe tomography of reactor pressure vessel steels: An analysis of data integrity. *Ultramicroscopy* **111**(6), 676–682.

Josefsson H, Liu F, Svensson JE, Halvarsson M & Johansson LG (2005). Oxidation of FeCrAl alloys at 500–900°C in dry O_2. *Mater Corros* **56**(11), 801–805.

Karahka M & Kreuzer HJ (2013). Field evaporation of oxides: A theoretical study. *Ultramicroscopy* **132**, 54–59.

Kingham DR (1982). The post-ionization of field evaporated ions: A theoretical explanation of multiple charge states. *Surf Sci* **116**, 273–301.

Kirchhofer R, Diercks DR, Gorman BP, Ihlefeld JF, Kotula PG, Shelton CT, Brennecka GL & Green DJ (2014). Quantifying compositional homogeneity in $Pb(Zr,Ti)O_3$ using atom probe tomography. *J Am Ceram Soc* **97**(9), 2677–2697.

Krämer S, Wells P, Oberdorfer C & Odette RG (2017). Correlative TEM and atom probe tomography - A case study on structural materials for fusion reactors. *Microsc Microanal* **23**(S1), 654–655.

Lambrinou K, Koch V, Coen G, Van den Bosch J & Schroer C (2014). Corrosion scales on various steels after exposure to liquid lead–bismuth eutectic. *J Nucl Mater* **450**(1), 244–255.

Langford RM & Petford-Long AK (2001). Preparation of transmission electron microscopy cross-section specimens using focused ion beam milling. *J Vac Sci Technol A* **19**(5), 2186–2193.

Larson DJ, Alvis RL, Lawrence DF, Prosa TJ, Ulfig RM, Reinhard DA, Clifton PH, Gerstl SSA, Bunton JH, Lenz DR, Kelly TF & Stiller K (2008). Analysis of bulk dielectrics with atom probe tomography. *Microsc Microanal* **14**(S2), 1254–1255.

Larson DJ, Foord DT, Petford-Long AK, Liew H, Blamire MG, Cerezo A & Smith GDW (1999). Field-ion specimen preparation using focused ion-beam milling. *Ultramicroscopy* **79**(1–4), 287–293.

Lim J, Hwang I & Kim J (2013). Design of alumina forming FeCrAl steels for lead or lead-bismuth cooled fast reactors. *J Nucl Mater* **441**(1–3), 650–660.

Lim J, Nam H, Hwang I & Kim J (2010). A study of early corrosion behaviors of FeCrAl alloys in liquid lead-bismuth eutectic environments. *J Nucl Mater* **407**(3), 205–210.

Liu F & Stiller K (2013). Atom probe tomography of thermally grown oxide scale on FeCrAl. *Ultramicroscopy* **132**, 279–284.

Lloyd MJ, Abernethy RG, Gilbert MR, Griffiths I, Bagot PAJ, Nguyen-Manh D, Moody MP & Armstrong DEJ (2019). Decoration of voids with rhenium and osmium transmutation products in neutron irradiated single crystal tungsten. *Scr Mater* **173**, 96–100.

Maier J, Pfeiffer B, Volkert CA & Nowak C (2016). Three-dimensional microstructural characterization of lithium manganese oxide with atom probe tomography. *Energy Technol* **4**(12), 1565–1574.

Miller MK & Forbes RG (2014). *Atom-Probe Tomography: The Local Electrode Atom Probe*. New York: Springer.

Mortazavi N, Geers C, Esmaily M, Babic V, Sattari M, Lindgren K, Malmberg P, Jonsson B, Halvarsson M, Svensson JE, Panas I & Johansson LG (2018). Interplay of water and reactive elements in oxidation of alumina-forming alloys. *Nat Mater* **17**(7), 610–617.

Müller G, Heinzel A, Konys J, Schumacher G, Weisenburger A, Zimmermann F, Engelko V, Rusanov A & Markov V (2002). Results of steel corrosion tests in flowing liquid Pb/Bi at 420–600 °C after 2000 h. *J Nucl Mater* **301**(1), 40–46.

Müller G, Heinzel A, Schumacher G & Weisenburger A (2003). Control of oxygen concentration in liquid lead and lead–bismuth. *J Nucl Mater* **321**(2), 256–262.

Müller G, Schumacher G & Zimmermann F (2000). Investigation on oxygen controlled liquid lead corrosion of surface treated steels. *J Nucl Mater* **278** (1), 85–95.

Nowok J (1982). Formation mechanisms of keying or pegging yttrium oxide and increased plasticity of alumina scale on FeCrAlY. *Oxid Met* **18**(1), 1–17.

Pint BA (1996). Experimental observations in support of the dynamic-segregation theory to explain the reactive-element effect. *Oxid Met* **45**, 1–37.

Pint B, Dryepondt S, Unocic K & Hoelzer D (2014). Development of ODS FeCrAl for compatibility in fusion and fission energy applications. *J Miner, Met Mater Soc* **66**(12), 2458–2466.

Santhanagopalan D, Schreiber DK, Perea DE, Martens RL, Janssen Y, Khalifah P & Meng YS (2015). Effects of laser energy and wavelength on the analysis of LiFePO(4) using laser assisted atom probe tomography. *Ultramicroscopy* **148**, 57–66.

Smialek JL, Jayne DT, Schaeffer JC & Murphy WH (1994). Effects of hydrogen annealing, sulfur segregation and diffusion on the cyclic oxidation resistance of superalloys: A review. *Thin Solid Films* **253**, 285–292.

Stiller K, Viskari L, Sundell G, Liu F, Thuvander M, Andrén HO, Larson DJ, Prosa T & Reinhard D (2012). Atom probe tomography of oxide scales. *Oxid Met* **79**(3–4), 227–238.

Thompson K, Lawrence D, Larson DJ, Olson JD, Kelly TF & Gorman B (2007). In situ site-specific specimen preparation for atom probe tomography. *Ultramicroscopy* **107**(2–3), 131–139.

Thuvander M, Weidow J, Angseryd J, Falk LK, Liu F, Sonestedt M, Stiller K & Andren HO (2011). Quantitative atom probe analysis of carbides. *Ultramicroscopy* **111**(6), 604–608.

Unocic KA, Chen Y, Shin D, Pint BA & Marquis EA (2018). STEM and APT characterization of scale formation on a La,Hf,Ti-doped NiCrAl model alloy. *Micron* **109**, 41–52.

Vayyala A, Povstugar I, Naumenko D, Quadakkers WJ, Hattendorf H & Mayer J (2020). A nanoscale study of thermally grown chromia on high-Cr ferritic steels and associated oxidation mechanisms. *J Electrochem Soc* **167**, 6.

Wallenius J (2019). Maximum efficiency nuclear waste transmutation. *Ann Nucl Energy* **125**, 74–79.

https://doi.org/10.1017/S1431927621000337 Published online by Cambridge University Press

Wallenius J & Bortot S (2018). A small lead-cooled reactor with improved Am-burning and non-proliferation characteristics. *Ann Nucl Energy* **122**, 193–200.

Wallenius J, Suvdantsetseg R & Fokau A (2012). ELECTRA: European lead-cooled training reactor. *Nucl Technol* **177**, 303–313.

Wang X, Hatzoglou C, Sneed B, Fan Z, Guo W, Jin K, Chen D, Bei H, Wang Y, Weber WJ, Zhang Y, Gault B, More KL, Vurpillot F & Poplawsky JD (2020). Interpreting nanovoids in atom probe tomography data for accurate local compositional measurements. *Nat Commun* **11**(1), 1022.

Weisenburger A, Mansani L, Schumacher G & Muller G (2014). Oxygen for protective oxide scale formation on pins and structural material surfaces in lead-alloy cooled reactors. *Nucl Eng Des* **273**, 584.

Weisenburger A, Müller G, Heinzel A, Jianu A, Muscher H & Kieser M (2011). Corrosion, Al containing corrosion barriers and mechanical properties of steels foreseen as structural materials in liquid lead alloy cooled nuclear systems. *Nucl Eng Des* **241**(5), 1329–1334.

Zhang J (2009). A review of steel corrosion by liquid lead and lead–bismuth. *Corros Sci* **51**(6), 1207–1227.

https://doi.org/10.1017/S1431927621000337 Published online by Cambridge University Press